Article

Not peer-reviewed version

Structural Characterization and Bioactivity of a Titanium(IV) -Oxo Complex Stabilized by Mandelate Ligands

Barbara Kubiak *, Tadeusz Muzioł, Grzegorz Wrzeszcz, Aleksandra Radtke, Patrycja Golińska, Tomasz Jędrzejewski, Sylwia Wrotek, Piotr Piszczek *

Posted Date: 19 March 2024

doi: 10.20944/preprints202403.1145.v1

Keywords: Titanium(IV) oxo-complex; α-hydroxyacid; mandelic acid; crystal structure; antimicrobial activity; cytotoxicity

Article

Structural Characterization and Bioactivity of a Titanium(IV) -Oxo Complex Stabilized by Mandelate Ligands

Barbara Kubiak [1,*], Tadeusz Muzioł [1], Grzegorz Wrzeszcz [1], Aleksandra Radtke [1], Patrycja Golińska [2], Tomasz Jędrzejewski [3], Sylwia Wrotek [3] and Piotr Piszczek [1,*]

[1] Department of Inorganic and Coordination Chemistry, Faculty of Chemistry, Nicolaus Copernicus University in Toruń, Gagarina 7, 87-100 Toruń, Poland (T.M.), (G.W.), (A.R.)
[2] Department of Microbiology, Faculty of Biological and Veterinary Sciences, Nicolaus Copernicus University in Toruń, Lwowska 1, 87-100 Toruń, Poland (P.G.)
[3] Department of Immunology, Faculty of Biological and Veterinary Sciences, Nicolaus Copernicus University in Toruń, Lwowska 1, 87-100 Toruń, Poland (T.J.), (S.W.)
* Correspondence: piszczek@umk.pl (P.P.), basiak0809@gmail.com (B.K)

Abstract: Research on titanium oxo complexes (TOCs) are usually focused on their structure and photocatalytic properties. Findings from these investigations spurred our interest in exploring also their potential biological activities. In this study, we focused on the synthesis and structure of a compound with the general formula $[Ti_8O_2(O^iPr)_{20}(man)_4]$ (**1**), which was isolated from the reaction mixture of titanium(IV) isopropoxide with mandelic acid (Hman) in a molar ratio of 4:1. The structure (**1**) was determined using single-crystal X-ray diffraction, while spectroscopic studies provided insights into its physicochemical properties. To assess the potential practical applications of (**1**), its microcrystals were incorporated into a polymethyl methacrylate (PMMA) matrix, yielding composite materials of the type PMMA + (**1**) (2 wt.%, 5 wt.%, 10 wt.%, and 20 wt.%). The next stage of our research involved the antimicrobial activity evaluation of the obtained materials. Investigations carried out demonstrated antimicrobial activity of pure (**1**) and its composites (PMMA + (**1**)) against both Gram-positive and Gram-negative strains. Furthermore, MTT tests conducted on the L929 murine fibroblast cell line confirmed the lack of cytotoxicity of these composites. Our study identified (**1**) as a promising antimicrobial agent, also for producing composite coatings.

Keywords: Titanium(IV) oxo-complex; α-hydroxyacid; mandelic acid; crystal structure; antimicrobial activity; cytotoxicity

1. Introduction

The wide interest in titanium(IV)-oxo complexes (TOCs) is associated with their structural diversity and photocatalytic activity [1,2]. These compounds have found applications in diverse technologies, including hydrogen production or water purification from organic pollutants [3,4]. Previous research has allowed the synthesis of TOCs with cores containing from 2 to 44 titanium atoms [5–12], with the largest group consisting of compounds with four- and six-nuclear cores [13–17]. The cores $\{Ti_aO_b\}$ of TOCs can be stabilized by alkoxide groups as well as carboxylate or phosphonate ligands, although β-diketonate, β-ketoester, and sulfonate ligands have also been employed [5,18,19]. The varied possibilities of carboxylate ligands coordination with titanium atoms [20] explain the fact that most of the works focus on investigations of Ti(IV)-oxo complexes stabilized with alkoxide and carboxylate ligands. Notably, the type of carboxylate ligand has a significant influence both on the $\{Ti_aO_b\}$ core structure and the oxo complex photocatalytic activity [5,7,21–26].

 doi:10.20944/preprints202403.1145.v1

Interest in Ti(IV)-oxo complexes also stems from their potential biomedical applications. Studies on the utilization of TOCs in photodynamic therapy [27] and as antimicrobial agents [5,13,24,28–30] are particularly significant. With the ongoing search for materials possessing bactericidal properties and the ability to prevent microbial growth, our research has concentrated on the latter aspect. Analysis of literature reports suggests that research on this issue is developing in three main directions. The first one involves the introduction of a heteroatom into the core structure, resulting in the synthesis of compounds containing {AgTi-oxo} or {AgTi} cores, which demonstrate favorable optical, antibacterial, and photothermal properties [29,30]. Luo et al. in their study on a complex featuring a $\{Ag_9Ti_4\}$ core stabilized by salicylate ligands proved, that its bacteriostatic efficacy against strains of *Staphylococcus aureus* and *Escherichia coli* was 94.51% and 95.42%, respectively, surpassing that of a comparable complex with a $\{Ag_2Ti\}$ core [30]. The improvement of the biocidal properties of the complex with the $\{Ag_9Ti_4\}$ core was achieved by the formation of a hydrogel $\{Ag_9Ti_4$-gel$\}$. Another approach to leveraging the antibacterial properties of Ti(IV)-oxo complexes was introduced in the research done by Svensson et al. [13]. In their study of the tetranuclear Ti(IV)-oxo complex ($\{Ti_4O_2\}$ core) stabilized with triclosan ligands, they capitalized on the compound's high susceptibility to hydrolysis processes, facilitating the release of an antibacterial agent (triclosan). According to this direction, Ti(IV)-oxo complexes are considered as carriers of bactericidal agents. The third strategy involves harnessing the photocatalytic activity of TOCs and capability to generate reactive oxygen species (ROS) [25,31]. In this case, the mechanism of biocidal action is associated with oxidative stress induced by the generated ROS. Our previous investigations confirmed the biocidal activity of $\{Ti_4O_2\}$ clusters stabilized with carboxylate ligands (such as 4-aminobenzoic acid, 4-hydroxybenzoic acid, and 9-fluorene carboxylate) [5,24,25]. Analysis of the electron paramagnetic resonance (EPR) spectra of these compounds confirmed the generation of O_2^- and O^- oxygen anions on the surface of both pure oxo complexes and composites prepared by dispersing the complexes in a poly(methyl methacrylate) (PMMA) matrix. It is worth noting that also $\{Ti_aO_b\}$ core structure influenced the antimicrobial activity of composites containing Ti(IV)-oxo complexes. Studying on oxo complexes with different core structures stabilized by 9-fluorene carboxylate ligands allowed for the observation of this effect. It was found that the biocidal activity of samples with $\{Ti_6O_4\}$ and $\{Ti_4O_2\}$ cores was higher than that of $\{Ti_6O_6\}$ and $\{Ti_3O\}$ systems, when irradiated with visible light [5]. To enhance the biocidal properties of synthesized TOCs, we decided to incorporate α-hydroxy carboxylate ligands known for their antimicrobial and anti-inflammatory properties [32–34] into their structure. Our goal was to develop a new, durable material with antimicrobial traits, responsive to light exposure in the UVA and visible range. The introduction of carboxylate ligands possessing α-hydroxy groups to TOCs structure increases their coordination possibilities with Ti(IV), resulting in the formation of more structurally stable systems in comparison to compounds stabilized by carboxylate groups [5,26,35]. Previous investigations proved the photocatalytic properties of TOCs stabilized with such α-hydroxy carboxylate ligands, as salicylate, 4-chlorosalicylate, 1-hydroxynaphthoate, citrate, and 2,5-dihydroxybenzoate [14,26,35–38]. Therefore, incorporating such ligands into oxo complexes' structure is expected to yield systems with biocidal activity as well. Considering the widespread application of mandelic acid (Hman) as a bactericidal agent in the cosmetic industry, its introduction to TOCs structure was intriguing [39,40]. Previous research on mandelic acid properties showed that prolonged skin exposure to Hman absorption may lead to redness, dryness, and excessive skin exfoliation [41,42]. Hence, investigations carried out in last years, focused on the synthesis and the evaluation of the biocidal action of Hman salts and their complex compounds [43,44]. The compounds synthesized in the reaction of titanium isopropoxide with mixtures of mandelic and benzohydroxamic acid [45] or mandelic and phenylphosphonic acid [46] typically form dimeric structures, wherein two titanium atoms ($\{Ti_2\}$) are connected solely by mandelic ligands (man). Schetter et al. synthesized titanium complexes with multinuclear cores, particularly $\{Ti_2\}$, $\{Ti_6\}$, $\{Ti_9\}$, stabilized by mandelic and tert-butoxide ligands [47]. Mandelic ligands play a critical role in the formation of $\{Ti_2\}$ dimer units through carboxylic and hydroxyl groups, also contributing to the creation of larger arrangements $\{Ti_6\}$ and $\{Ti_9\}$. It is worth noting that described compounds have no

 doi:10.20944/preprints202403.1145.v1

{Ti_aO_b} cores, so the oxo complex we have synthesized is completely new from the structural point of view.

In this paper, we present the results concerning the synthesis of a structurally stable Ti(IV)-oxo complex with the general formula [$Ti_8O_2(O^iPr)_{20}(man)_4$] (**1**). The novel {$Ti_8O_2$} core exhibits a unique topology characterized by a plethora of labile isopropoxide ligands and a limited number of oxo bridges. Our objective was to evaluate the biocidal activity of the synthesized compound (**1**) and the composite films formed by dispersing (**1**) in the PMMA matrix (PMMA + (**1**)).

2. Results

2.1. Structure of (1) Oxo-Complex

The octanuclear cluster {Ti_8O_2} of the oxo complex (**1**) is formed in unprecedented way, around a central tetranuclear {Ti_4O_2} unit, with two lateral dimers {Ti_2} attached to it via O1 and O11 mandelate ligand bridges (Figure 1). In these lateral dimers, Ti3 and Ti4 cations are connected by an O61 isopropionate anion and an O13 hydroxyl group from the O11 mandelate anion, resulting in a very short intermetalic distance between them, measuring 3.2486(15) Å (Table S1). The central {Ti_4O_2} core consists of two Ti1 and two Ti2 cations forming a slightly distorted rhombus, with Ti1-Ti2 distances of 3.1036(10) and 3.1940(10) Å, respectively. This arrangement is stabilized by two O10 μ_3-oxo bridges connecting two Ti1 cations and one Ti2 cation, along with two O31 isopropionate anions and two O3 hydroxyl groups from the O1 mandelate anion. The O10 oxo group forms one short bond and two much longer bonds, leading to a topology distinct from previously reported {Ti_4O_2} cores where titanium cations are coupled by one μ_4-oxo and one μ-oxo bridge [7] (Figure S1). Ti(IV) titanium cations exhibit significant differences in coordination number and coordination sphere content (refer to Table S2). Ti1 is situated in an octahedral environment with a terminal O21 and bridging O31 O^iPr anions, as well as O1 and O2 oxygen atoms from the mandelate anion forming a chelate ring, along with two O10 oxo anions. The octahedral coordination sphere of Ti2 comprises two terminal (O41 and O51) and one bridging (O31) isopropionate anions, one O10 oxo anion, and O3 and O12 oxygen atoms from two α-hydroxyacid anions. Similarly, lateral Ti3 exhibits an octahedral coordination sphere, consisting of two terminal (O71 and O81) and one bridging (O31) O^iPr anions, along with three oxygen atoms from bridging mandelate anions (O11 and O13 forming a chelate ring, while the O2 hydroxyl group bonds with the central unit). Finally, the outermost Ti4 cation is pentacoordinated, with three terminal OiPr anions (O91, O101, O111), one bridging O61 isopropionate anion, and one bridging O13 hydroxyl group from the mandelate anion. In the case of coordinatively unsaturated titanium, a geometry parameter ($\tau5 = 0.60$) [48] indicates a significantly distorted trigonal bipyramid configuration.

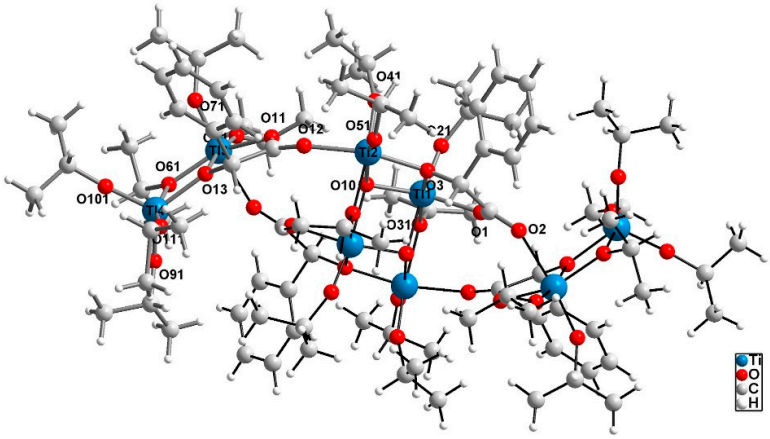

Figure 1. Structure of [$Ti_8(\mu_3\text{-}O)_2(\mu\text{-}O^iPr)_4(O^iPr)_{16}(man)_4$] (**1**) as a ball and stick model with hydrogen atoms omitted for the clarity of the figure. The structure presents only the main conformations. Atom

 doi:10.20944/preprints202403.1145.v1

labels for titanium and oxygen atoms are given. The asymmetric part is presented with bonds in medium grey and the part related by inversion center in black.

The crystal network does not exhibit any cavities containing uniformly distributed octanuclear clusters (Figure 2). Hirshfeld surface analysis reveals that weak interactions dominate the landscape of the formed interactions (Figure 3). Specifically, H…H interactions constitute 96.8% of the intermolecular contacts, with the remaining 3.2% attributed to H…C contacts. Despite careful analysis, no intermolecular hydrogen bonds were observed, while several intramolecular C-H…O hydrogen bonds were identified. This suggests that oxygen atoms are buried and inaccessible to hydrogen atoms from adjacent clusters. Moreover, the high propanalate/mandelate ratio (5:1) results in only one π-π interaction, occurring between the strongly inclined C14 phenol ring and the Ti3O11 five-membered chelate ring. Summarizing, we synthesised stable complex with the unprecedented core structure $\{Ti_8O_2\}$, which may interact with biomolecules in the cell via external and easily accessed unsaturated Ti4 cation, as well as through weak non-covalent van der Waals forces.

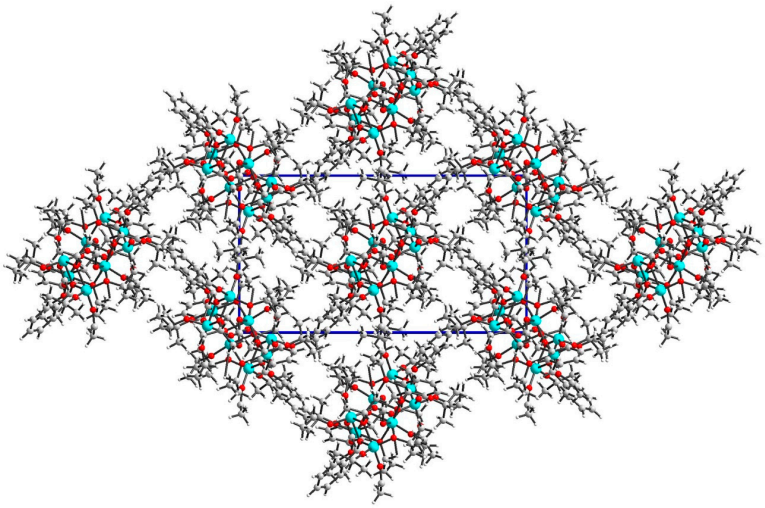

Figure 2. Crystal network of (**1**) along c axis shows ab layers.

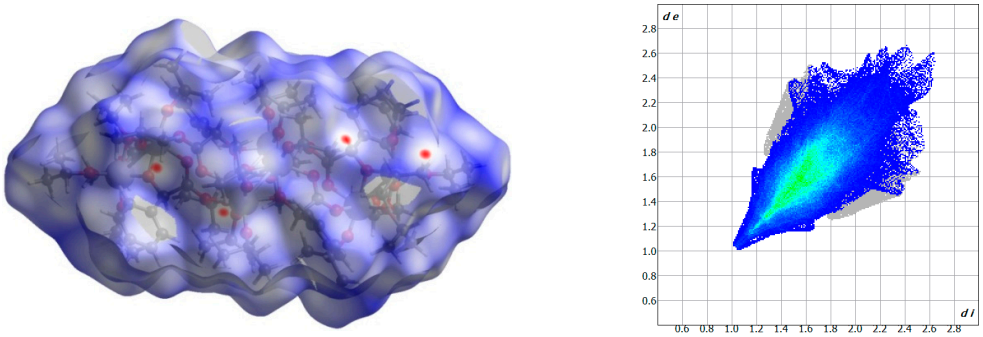

a *b*

 doi:10.20944/preprints202403.1145.v1

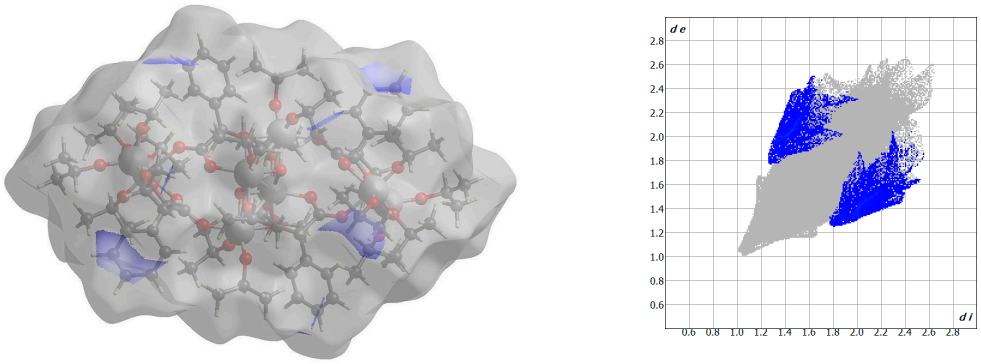

Figure 3. Hirshfeld surfaces and fingerprints of selected interactions created in the crystal network of (**1**): Hirshfeld surface (a) and fingerprint (b) for H…H (96.8%), Hirshfeld surface (c) and fingerprint (d) for H…C (3.2%). In brackets, there is given surface area included as a percentage of the total surface area.

*2.2. Spectral Characterization of (**1**) and Its Composite with Poly(Methyl Methacrylate)*

The objective of spectral studies was to determine the structural stability, including susceptibility to hydrolysis processes, and physicochemical properties of both the complex and its composite formed by dispersing micrograins of this compound in a non-toxic poly(methyl methacrylate) matrix (PMMA + (**1**)). Research on composite systems aimed to assess their practical potential as antimicrobial coatings. To this end, PMMA + (**1**) composite samples were prepared, with 2 wt.%, 5 wt.%, 10 wt.%, and 20 wt.%. Figure 4 illustrates the XRD patterns of the (**1**) sample recorded before and after immersion in distilled water for 72 hours. Both diffractograms were compared to the pattern calculated in [49]. Analysis of the XRD data revealed no significant differences in patterns before and after immersion in water. The resemblance between these diffractograms indicates that the core structure was preserved, and no significant transformation towards crystalline TiO_2, amorphous forms, or other crystalline species related to rearrangement of the titanium co-ordination spheres and topology was detected. The structural stability of (**1**) was further confirmed using IR spectroscopy (Figure 5). The comparison of IR spectra of samples before and after immersion in water showed no changes. There were no alterations in the intensity and position of bands within the ranges of (a) 1624-1450 cm^{-1}, which are associated with the vibrations ν(CC), ν_{as}(COO), and ν_{s}(COO), (b) 900-1200 cm^{-1}, assigned to the ν(O-CR) vibrations, and (c) bands appearing below 900 cm^{-1}, indicated titanium-oxo bridges.

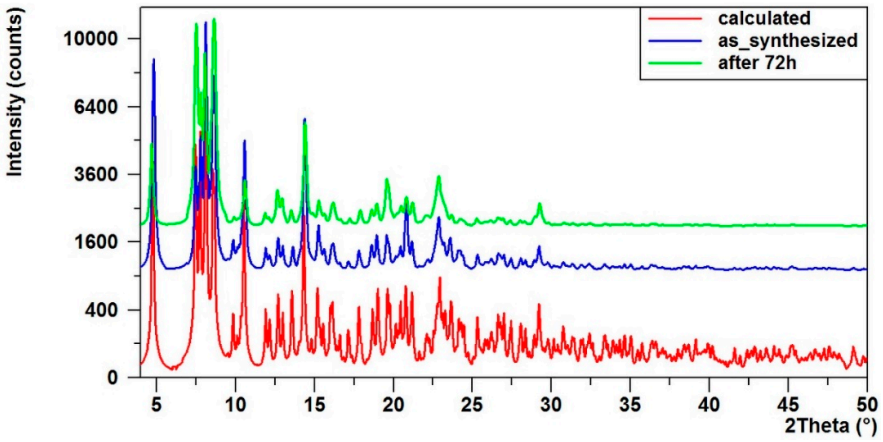

Figure 4. The powder diffractograms: calculated using our model (red), the synthesized complex (blue), the sample after being immersed in distilled water for 72 h (green) in the range of 4 – 50° 2θ.

 doi:10.20944/preprints202403.1145.v1

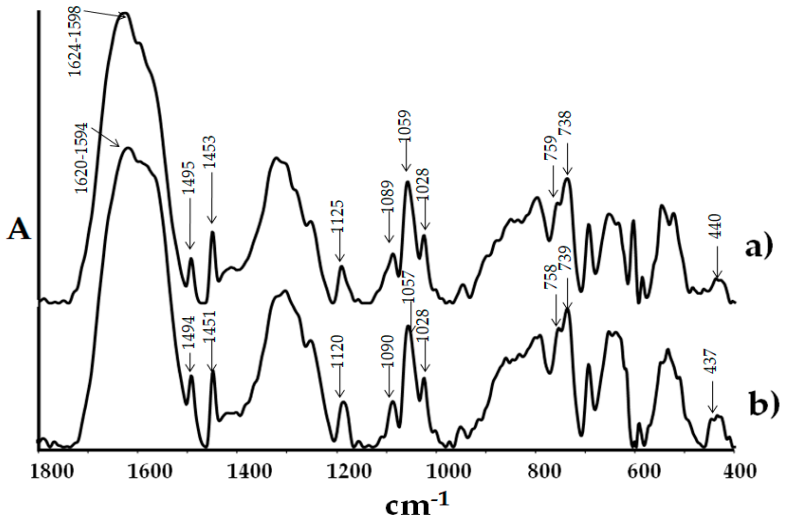

Figure 5. IR spectrum of structure (**1**) before (a) and after 72h contact with water (b).

The presence of (**1**) in the polymer matrix was confirmed using SEM EDX (Table 1). Titanium peaks are observed in each composite sample, and the percentage of titanium increases with the (**1**) sample concentration. To verify the absence of structural changes in (**1**) upon incorporation into the PMMA matrix, we compared the Raman spectra of the oxo complex (**1**), the composite of PMMA + (**1**) 20 wt.%, and pure PMMA polymer (Figure 6). The results obtained suggest that the structure of the compound remains unchanged upon introduction into the matrix.

Table 1. SEM EDX data for composites PMMA + (**1**). All values are given in mass percent (%).

Composite	C	O	Al	Ti
PMMA	26.10	72.23	1.67	-
PMMA + (**1**) 2wt.%	28.27	71.00	0.45	0.27
PMMA + (**1**) 5wt.%	24.75	66.45	0.59	8.21
PMMA + (**1**) 10wt.%	19.02	67.24	0.52	13.22
PMMA + (**1**) 20wt.%	18.77	58.68	0.48	22.07

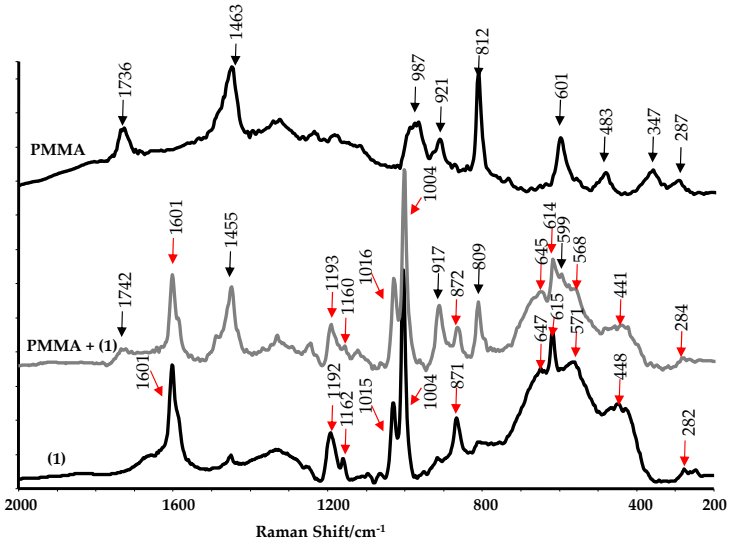

 doi:10.20944/preprints202403.1145.v1

Figure 6. Raman spectra of (**1**), PMMA + (**1**) 20 wt.%, and pure PMMA.

The EPR spectra of (**1**) powders and cut composite foil were recorded to identify paramagnetic species on the surface of the synthesized materials (Table 2 and Figure S2). Pure PMMA polymer exhibited no EPR signal. Paramagnetic centers were detected in all samples of PMMA + TOCs composites, as well as in the spectrum of pure (**1**). Generally, the signals in the EPR spectra were weak, particularly for composites with low (n = 2, 5, 10) wt.% admixture of oxo-titanium(IV) complexes (although ROS signals were detected, Table 2). Consequently, only the EPR spectra of the pure (**1**) sample and the composite sample containing 20 wt.% of oxo-titanium(IV) complex grains were analyzed in detail. The spectra registered for pure (**1**) and the composite of PMMA + (**1**) 20 wt.% are presented in Figure S2. Analysis of the EPR spectra of the aforementioned samples demonstrated that natural photoexcitation of their surface, i.e., generated without additional UV-Vis lamp radiation, led to the formation of ROS. Additionally, it is worth noting that both O^- and O_2^- paramagnetic species were generated by the PMMA + TOCs composite. Interestingly, the O_2^- radical was also generated in the pure substrate.

Table 2. EPR data for powdered TOC and PMMA + (**1**) composite samples. The samples were exposed to visible light prior to measurement.

Sample	g-factor	Species
(**1**)	2.025, 2.011,2.003	O_2^-
	1.992	Ti(III)
PMMA	-	-
PMMA + (**1**) 5 wt.%	2.010, 2.002	O_2^-
	2.005, 2.000	O^-
	1.992	Ti(III)
PMMA + (**1**) 10 wt.%	2.025, 2.010, 2.000	O_2^-
	2.016	O^-
	1.992	Ti(III)
PMMA + (**1**) 20 wt.%	2.025, 2.010, 2.002	O_2^-
	2.016, 2.005, 2.000	O^-
	1.992, 1.972	Ti(III)

*2.3. Antimicrobial Activity of (**1**) and Its Composites*

The subsequent phase of our research involved evaluating the biocidal activity of both (**1**) and the PMMA + (**1**) composite. These assessments were conducted against Staphylococcus aureus and Escherichia coli bacteria, as well as Candida albicans fungi. The results, as depicted in Table 3, reveal that the complex (**1**) exhibited significant antimicrobial activity, even at low concentrations. According to ISO 22196:2011 standard, suspension exhibit biocidal effect when the R value is ≥ 3. In the case of (1) suspensions, the R value for Gram-negative bacteria ranged from 5.7 to 6.0, while for Gram-positive bacteria, it varied from 4.2 to 6.2. Microbiological activity against Candida albicans was only apparent with a 20% (w/v) addition of (**1**). Non-porous surfaces are considered bactericidal when the R ≥ 2. Microbiological tests of composite samples (PMMA + (**1**)) exhibited outstanding activity against both E. coli and S. aureus bacteria across all tested concentrations of TOCs (2 wt.%, 5 wt.%, 10 wt.%, and 20 wt.%), as detailed in Table 3. Even at a modest (**1**) content of 2 wt.%, the composite displays effective activity against E. coli bacteria (R ≥ 2). In terms of S. aureus bacteria, the R values ranging from 4.7 to 5.1. It is noteworthy that the tested composites do not diminish the count of C. albicans cells.

 doi:10.20944/preprints202403.1145.v1

Table 3. Antimicrobial activity of TOC and PMMA + n(**1**) composites; value R ≥ 2 determines biocidal activity for composites and R ≥ 3 for the (**1**) suspension.

No.	Samples	Microorganisms				
		E. coli ATCC 8739	*E. coli* ATCC 25922	*S. aureus* ATCC 6538	*S. aureus* ATCC 25923	*C. albicans* ATCC 10231
1	(**1**) 2 wt.%	6.0 (>99.99%)	6.0 (>99.99%)	4.2 (>99.99%)	5.4 (>99.99%)	0 (0%)
2	(**1**) 5 wt.%	6.0 (>99.99%)	5.7 (>99.99%)	5.9 (>99.99%)	6.0 (>99.99%)	0.3 (53.20%)
3	(**1**) 10 wt.%	6.0 (>99.99%)	6.0 (>99.99%)	6.2 (>99.99%)	6.0 (>99.99%)	0.9 (87.45%)
4	(**1**) 20 wt.%	6.0 (>99.99%)	6.0 (>99.99%)	6.5 (>99.99%)	5.7 (>99.99%)	6.7 (>99.99%)
5	PMMA	none (0%)	none (0%)	none (0%)	none (0%)	none (0%)
6	PMMA + (**1**) 2 wt.%	2.0 (99.00%)	3.1 (>99.90%)	4.7 (>99.99%)	5.1 (>99.99%)	+0.9 (+87.41%)
7	PMMA + (**1**) 5 wt.%	3.1 (>99.90%)	4.9 (>99.99%)	4.7 (>99.99%)	5.1 (>99.99%)	+0.82 (+84.86%)
8	PMMA + (**1**) 10 wt.%	4.9 (>99.99%)	3.9 (>99.90%)	4.7 (>99.99%)	5.1 (>99.99%)	+0.8 (+84.20%)
9	PMMA + (**1**) 20 wt.%	4.9 (>99.99%)	4.7 (>99.99%)	4.7 (>99.99%)	5.1 (>99.99%)	+0.7 (+80.05%)

*2.6. Cytotoxicity of PMMA + (**1**) Composites*

The potential cytotoxicity of the tested specimens was assessed using MTT assays and analysis of SEM images. The purpose of this study is to determine whether compound (**1**) can damage human or animal cells. A material is considered non-cytotoxic if cell viability is greater than 70%. The results of the MTT assays showed that the level of cell viability measured for the reference PMMA samples was comparable to the values received for specimens containing mandelic ligands in all tested concentrations.This effect was observed in both 24 and 72 hours of incubation time. Importantly, these results also demonstrated that with an increase in the incubation time, more L929 fibroblasts proliferated on all the tested specimens (Figure 7).

Figure 8 presents selected images of L929 cells cultured on the PMMA specimens containing mandelic ligands at a concentration 2 (A, B, F) and 20 wt.% (C, D, E). Firstly, analysis of these micrographs confirmed the results from the MTT assays indicating that L929 fibroblasts effectively attached to the surfaces and the number of the growing cells increased over time (compared Figure 8 A-B and 8 C-D). After 72 hours, the fibroblasts covered the sample surface area at a significantly higher density. Importantly, the elongated shape of the cells was observed already after 24 hours of culture indicating their normal adhesion with few cytoplasmic projections at the cell edges that allowed also cells to attach to the surface of specimens (Figure 8F).

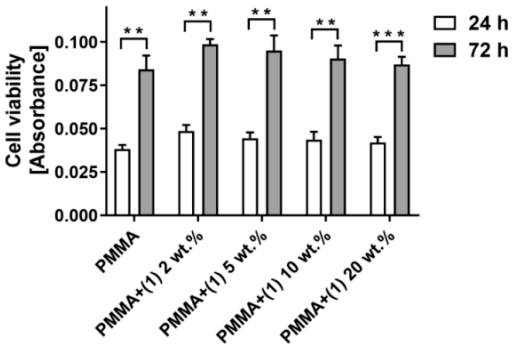

Figure 7. The viability of L929 fibroblasts growing on the surfaces of PMMA reference samples and PMMA specimens containing mandelic ligands at a concentration of 2 wt.%, 5 wt.%, 10 wt.%, and 20 wt.%. The cells were cultured on the samples for 24 and 72 hours. The absorbance values are expressed as means ± S.E.M of four independent experiments. Asterisks indicate significant statistical differences in the cell viability between 24 and 72 hours (*** $p < 0.001$; ** $p < 0.01$).

 doi:10.20944/preprints202403.1145.v1

After 72 hours, the number of cytoplasmic projections at the cell periphery had increased, and after getting into closer proximity to the neighbouring cells they started forming cell–cell contacts (Figure 8E). The cytoplasmic projections called as filopodia play a fundamental role in cell attachment, migration, proliferation, and cell-cell interaction [50,51]. The results from MTT assays and SEM analysis showed that the tested specimens containing MA did not affect the morphology of L929 fibroblasts and did not reduce their viability.

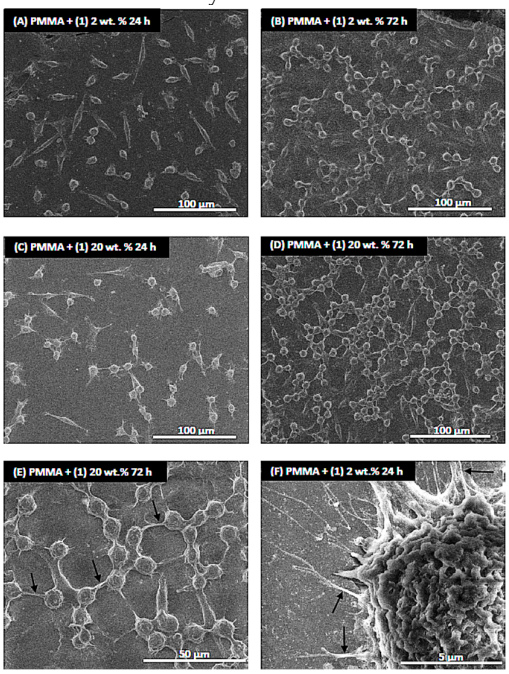

Figure 8. Scanning electron microscopy images of L929 cells cultured on the surfaces of PMMA specimens containing mandelic ligands at a concentration 2 (A, B, F) and 20 wt.% (C, D, E). The type of samples, incubation time and scales of the images were presented in the figures. Black arrows in Figure E indicate cytoplasmic projections spread between the cells, whereas those in Figure F present cytoplasmic projections attaching the cells to the surface.

3. Discussion

The crystals with the general formula $[Ti_8O_2(O^iPr)_{20}(man)_4]$ (**1**) were obtained from a reaction mixture containing titanium isopropoxide and mandelic acid in a 4:1 molar ratio at room temperature, using tetrahydrofuran as a solvent. Single crystal X-ray Diffraction analysis confirmed that the structure of (**1**) consists of a $\{Ti_8O_2\}$ core stabilized by isopropoxide and mandelate ligands (Figure 1). Previous studies have reported the occurrence of $\{Ti_8O_8\}$ cores in octanuclear Ti(IV)-oxo complexes, composed of eight-membered rings where Ti atoms are surrounded by μ-O and μ-carboxyl bridges [52–56]. Czakler et al. synthesized a compound with a $\{Ti_8O_2\}$ core consisting of two $\{Ti_4O\}$ units bridged by two μ_3-O atoms [57]. The structure of (**1**) is more intricate as its core comprises a central $\{Ti_4O_2\}$ unit and two lateral dimers ($\{Ti_2\}$). This reported structure presents a novel unprecedented core among titanium oxo complexes (TOCs), stabilized by two μ_3-O bridges and mandelate anions forming bridges, and for Ti1 and Ti3, also a five-membered chelate ring. To verify the structural stability of (**1**) both in aqueous solutions and after its integration into the polymer matrix, spectroscopic analyses were conducted on powder samples after contact with water (employing XRD and IR methods) and samples of the PMMA + 20 composite (**1**) (with Raman spectra recorded). TOCs are recognized for their vulnerability to structural destabilization and hydrolysis. Compounds prone to hydrolysis find limited utility, particularly in applications involving exposure to aqueous environments. Existing literature suggests that incorporating carboxylates, phenols, phosphonates, and catechols into the coordination sphere can bolster the stability of such structures [12,58–60]. Our research affirms that the obtained compound maintained its structure when exposed

 doi:10.20944/preprints202403.1145.v1

to an aqueous environment. This is supported by the absence of notable alterations in the X-ray diffraction patterns and IR spectra before and after exposure to water. Examination of the Raman spectra of PMMA + (**1**) 20 wt.% composite samples revealed that the compound (**1**) preserved its structure subsequent to its integration into the polymer matrix. The pivotal focus of this stage of the research centered on evaluating the photoactivity of both the pure oxo complex and its composites. Utilizing electron paramagnetic resonance (EPR) facilitated the detection of reactive oxygen species (ROS) generated on the surface of samples previously exposed to visible light. Considering literature data, it is reasonable to assume that upon photoexcitation of the samples, Ti(III) and ROS would be initially generated on their surfaces [61–65]. The formation of O_2^- and O^- type paramagnetic centers involves electron removal and stabilization of the radical formed by reducing Ti(IV) to Ti(III) [61,62]. The maximum g-factor for O_2^- exceeds that of O^- species [63]. In the EPR spectrum of (**1**), characteristic anisotropic signals for the O_2^- radical were identified (Table 2, Figure S2(a)). Detecting titanium(III) is not straightforward; in this case, a weak and broad signal, nearly at the noise level, may be present (Figure S2(a), Table 2). The EPR spectra of PMMA + (**1**) composites are more intricate and contain numerous overlapping lines (Figure S2). The spectra of all composites are akin, except for variations in intensity. Weaker lines are indiscernible for samples containing minor admixtures (2 and 5%) of the titanium(IV) complex. In the spectrum of PMMA + (**1**) 20% wt.%, distinct signals of both ROS, i.e., O_2^- and O^-, as well as Ti(III) are evident (Table 2, Figure S2(b)). Some lines, particularly for g_2 and g_3 of both oxygen species, may overlap. Individual lines are relatively broad due to the high content of (**1**) and potential high paramagnetic center concentration, resulting in line broadening via exchange interactions. In contrast to similar TOCs composites with PCL [25,66], Ti(III) was discerned on the surface of the investigated composite material (Table 2, Figure S2(b)). Due to a positive spin-orbit coupling constant, Ti(III) exhibits EPR signals at g-values below 2.0 [25,61–66]. The first signal, with a g-factor of 1.992, is clearly visible, while the second, with a lower g-factor, approximately 1.972, is very weak and broad.

Elucidating the biocidal attributes of the synthesized oxo complex (**1**) and its composite PMMA + (**1**) involves considering two factors: (i) the photocatalytic capability of the oxo complex, and (ii) structural factors, particularly the formation of chelate rings. The photocatalytic prowess of (**1**) is associated with the generation of reactive oxygen species (ROS) upon exposure to visible light, as confirmed by EPR tests. Introducing ROS to a bacterial cell induces oxidative stress, leading to impairment of cellular lipids, proteins, and nucleic acids, ultimately resulting in the demise of the microorganism [67–70]. The antimicrobial efficacy can also be linked to the compound's structure, especially the formation of chelate rings and surface hydrophobicity (as observed in the Hirshfeld surface). According to Tweedy's chelation theory and Overtone's concept, coordination diminishes the metal ion's polarity by overlapping ligand orbitals and partially sharing the positive charge with donor groups [71]. The enhanced delocalization of π-electrons in the chelate ring augments the compound's lipophilic nature. This increased lipophilicity promotes the solubility of lipids in the cell membrane upon contact with the oxo complex grains, leading to irreversible damage to the membrane and cell functions [71]. Literature reports suggest a correlation between electron density and antimicrobial activity, with chelation increasing the electron density of the central ion [72]. It should be emphasized that the synergy of mechanisms involving the generation of ROS and effects related to the presence of a chelating ring can be considered as the primary mechanism only in the case of antimicrobial action of (**1**), where the entire surface of the oxo complex grain comes into contact with the microbial suspension. However, in composite materials, the grains are surrounded by a polymeric matrix exhibiting weaker biocidal activity, solely due to ROS generation on their surface. This is confirmed by the data analysis presented in Table 3, indicating that the activity of the PMMA + (**1**) composite is weaker compared to the pure compound.

Studies on the antimicrobial activity of mandelic acid (Hman) revealed that the minimum inhibitory concentration (MIC) required to inhibit the growth of S. aureus and E. coli strains fell within the range of 0.18-0.23% [43,73]. In the case of crystalline powder tests of (**1**), the mandelic ligand content in the suspension of the studied sample was 0.013%, 0.034%, 0.069%, and 0.14% for concentrations of 2%, 5%, 10%, and 20% (w/v), respectively. It suggests that the antibacterial activity

 doi:10.20944/preprints202403.1145.v1

of (**1**) against S. aureus and E. coli strains is superior to mandelic acid. When evaluating the biocidal properties of the tested samples, it is essential to consider that, according to ISO standards, a suspension is deemed bactericidal when equal or above 99.90% of microorganisms are inhibited (reduction index (R)≥3), while for non-porous surfaces is ≥2. It seems that the incorporation of (**1**) grains into a polymer matrix resulted in a decrease in antimicrobial activity when compared with suspensions, but still biocidal activity was achieved on the required level according to ISO 22196:2011 standard (Table 3). An interesting comparison can be made with the results obtained by Luo et al. for compounds containing {Ag_9Ti_4} cores and also hydrogel samples type {Ag_9Ti_4}-gel. Antimicrobial activity assessments showed that {Ag_9Ti_4} crystals exhibited antibacterial activity on the level S. aureus 94.51%, E. coli 95.42%, respectively [30]. For comparison, our oxo complex (**1**) showed an inhibitory effect of >99.99% for both strains of tested samples containing already 2% (w/v) in studied suspension. The hydrogel of {Ag_9Ti_4}-gel exhibited bactericidal effects versus S. aureus 99.6% and E. coli 99.95% [30]. The authors suggest that the increase in antimicrobial activity is a result of the synergistic effect of the {Ag_9Ti_4} cluster and polydopamine, added as a cross-linking agent in hydrogel formation. In the case of our composites, even a 2% addition of TOCs reduced the number of S. aureus by 99.00% and E. coli by 99.99%, it is in line with the ISO standard for bactericidal properties, which states that the number of microorganisms must be reduced by ≥99% (R ≥2).

Testing the cytotoxicity of the obtained materials was a very important aspect from the application point of view. In addition to antimicrobial properties, the obtained surfaces should not exhibit cytotoxicity towards fibroblast cells. This guarantees safety in case of contact with human skin. We presume that the topology affects the cytotoxic activity. The exact mechanism of titanium clusters cytotoxicity is not known and it is not clear if it is related to DNA intercalation [74]. Studies show that the cytotoxic effect is related to the stability of the compound. Hydrolyzed molecules are characterized by strong cytotoxic activity. L(OEt)Ti-O-Ti(OEt)L being product of partial hydrolysis of [$L(OEt)_2Ti$] show strong cytotoxicity despite bulky substituents [75]. The compound we obtained is characterized by high stability and low cytotoxicity, which confirms this theory.

4. Materials and Methods

4.1. Materials

Titanium(IV) isopropoxide (Aldrich, St. Louis, MO, USA) and mandelic acid (Warchem, Warsaw, Poland) were commercially purchased and used without additional purification. Tetrahydrofuran (THF) was distilled before usage and stored in an argon atmosphere. The synthesis of Ti(IV) oxo-complexes was conducted in an inert gas atmosphere (Ar) at room temperature (RT).

4.2. Synthesis of Ti(IV) Oxo-Complex (α-TOCs) and Preparation of PMMA/TOC COMPOSITES

4.2.1. The Synthesis of [$Ti_8O_2(O^iPr)_{20}(man)_4$] (1)

0.13 g of mandelic acid (0.875 mmol) was added to the solution of 1 mL of titanium(IV) isopropoxide (3.5 mmol) in 2 mL of THF, leading to clear yellow solution. The solution was left for crystallization (3 days).The yield basing on acid: 66% (0.62 g).Anal. Calc. for $C_{92}H_{168}O_{34}Ti_8$:C, 50.18; H, 7.63; Ti,17.45. Found: C, 50.09; H, 7.58; Ti, 17.54. ^{13}C NMR (solid state, 295 K, δ[ppm]): 9.75 (CH3), 25.4, 30.1 (CH), 60.1, 71.3 ((Ph)C(Ph)), 90.7, 130.7, 139.6, 182.3, (C(Ph)), 198.3, 209.4 (COO).

4.2.2. PMMA/TOCs Composites Preparation

The synthesized Ti(IV)-oxo cluster (TOC) were prepared by adding the TOCs (ca. 0.025, 0.062, 0.12 or 0.25 g of (**1**) TOC dispersed in 5 mL of THF) to the poly(methyl methacrylate) (PMMA) solution (1.0 g of PMMA dissolved in 10 mL of THF) to receive materials containing 2, 5, 10 and 20% of TOC. After 150 min in an ultrasonic bath, dispersions were poured into a glass Petri dish and left for the evaporation of the THF at RT in glove box.

 doi:10.20944/preprints202403.1145.v1

4.3. Analytical Methods

4.3.1. Structural and Spectroscopic Characterization of TOCs

The vibrational spectra of synthesized compounds (crystals) were registered using: (a) IR spectrophotometry (Perkin Elmer Spectrum 2000 FTIR spectrophotometer (400–4000 cm^{-1} range, KBr pellets)), and (b) Raman spectroscopy (RamanMicro 200 spectrometer (PerkinElmer, Waltham, MA, USA)). Raman spectra were recorded using a laser with the wavelength 785 nm, with a maximum power of 350 mW, in the range 200–3200 cm^{-1}, and a 20 x 0.40/FN22 objective lens and an exposure time of 15 s each time. The ^{13}C NMR spectra in the solid phase were recorded on a Bruker Advance 700 (Madison, WI, USA) 700 MHz spectrometer, with a spectral width of 76,923.08 Hz and 4096 complex points. Elemental analyses were performed on Elemental AnalyserVario Macro CHN (ElementarAnalysensysteme GmbH, Langenselbold, Germany).

4.3.2. Single Crystal X-ray Diffraction Measurement

The diffraction data were collected at 100 K on Rigaku XtaLAB Synergy (Dualflex) diffractometer with HyPix detector with monochromated CuKα X-ray source (λ= 1.54184 Å). The data processing and the numerical absorption correction were performed using CrysAlis Pro [76]. The structure was solved by the direct methods and refined with full-matrix least-squares procedure on F^2 (SHELX-97 [77]). Heavy atoms were refined with anisotropic displacement parameters, whereas hydrogen atoms were assigned at calculated positions with thermal displacement parameters fixed to a value of 20% or 50% higher than those of the corresponding carbon atoms. A disorder was observed for O31 (0.5:0.5) and O111 (0.6: 0.4) isopropionate anions. Some restraints on geometry (DFIX) and thermal parameters (ISOR) of those disordered anions were applied to assure a stable refinement process. All figures were prepared in DIAMOND [78]. The results of the data collections and refinement have been summarized in Table 4, selected bond lengths and angles are presented in Table S1.CCDC 2310326 contains the supplementary crystallographic data for (**1**). These data can be obtained free of charge from The Cambridge Crystallographic Data Centre via www.ccdc.cam.ac.uk.data_request/cif.

Table 4. Crystal data and structure refinement for (1).

Empirical formula	C_{92} H_{164} O_{34} Ti_8 (**1**)
Formula weight	2197.42
Temperature	100(2) K
Wavelength [Å]	1.54184
Crystal system	Monoclinic
Space group	$P2_1/c$
Unit cell dimensions [Å] and [°]	a = 19.9172(6)
	b = 12.3935(3)
	c = 24.4651(8)
	α = 90
	β = 111.483(4)
	γ = 90
Volume [$Å^3$]	5619.5(3)
Z, calculated density [Mg/m^3]	2, 1.299
Absorption coefficient [mm^{-1}]	5.193
F(000)	2328
Crystalsize [mm^3]	0.220 x 0.180 x 0.080
Theta range for data collection [°]	2.384 to 74.492
Index ranges	-24<=h<=24
	-15<=k<=14
	-30<=l<=21
Reflections collected/unique	44138/ 11218 [R(int) = 0.0943

 doi:10.20944/preprints202403.1145.v1

Completeness to theta	67.684° 99.9 %
Absorption correction	Gaussian
Max. and min. transmission	1.000 and 0.414
Refinementmethod	Full-matrix least-squares on F2
Data / restraints / parameters	11218 / 35 / 654
Goodness-of-fit on F2	1.054
Final R indices [I>2sigma(I)]	R1[a] = 0.0865, wR2[b] = 0.2451
R indices (all data)	R1[a] = 0.1092, wR2[b] = 0.2674
Largest diff. peak and hole	0.766 and -0.915 e·Å^{-3}

[a] $R1 = \Sigma||F_o| - |F_c||/\Sigma|F_o|$ [b] $wR2 = [\Sigma w(F_o^2 - F_c^2)^2/\Sigma(w(F_o^2)^2)]^{1/2}$.

4.3.3. X-Ray Diffraction of Powders

Powder experiments were performed on Rigaku XtaLAB Synergy (Dualflex) diffractometer with HyPix detector with monochromated CuKα X-ray source (λ= 1.54184 Å) working in the powder diffraction mode. The data were collected in the range 4-50°2θ with exposure time 240 s per frame.

4.3.4. Characterization of PMMA +TOCs Composite Materials

The chemical composition of the produced composite films was determined using an energy-dispersive X-ray spectrometer (EDS, Quantax 200 XFlash 4010, Bruker AXS, Karlsruhe, Germany). The maximum of absorption for samples PMMA + (1) were also registered with the use of UV–Vis DRS method. The resulting composite materials had a thickness of approximately 50 μm and were characterized using Raman.

4.3.5. The Electron Paramagnetic Resonance (EPR) Spectroscopy

EPR has been used in order to the confirmation of reactive oxygen species formation on the surface of the investigated samples. Measurements were carried out using an X band EPR SE/X-2541M spectrometer (Radiopan, Poznań, Poland) with a 100 kHz modulation. The microwave frequency was monitored with a frequency meter. The magnetic field was measured with an automatic NMR-type JTM-147 magnetometer (Radiopan, Poznań, Poland). Measurement conditions: microwave frequency: ca. 9.33 GHz; modulation amplitude: 0.25-1 mT; sweep: 20-50 mT; sweep time: 4 min.; time constant: 0.1 s; receiver gain: 4 x 10^5. The measurements were performed for powder of substrate and cutted films of PMMA + TOCs composites at room temperature.

4.4. Studies of the Biological Activity of Synthesized Materials

4.4.1. Antimicrobial Activity of PMMA + (**1**) Composites and Powder (**1**)

Antimicrobial activity of the samples was determined against Gram-negative (*Escherichia coli* ATCC 25922, *Escherichia coli* ATCC 8739) and Gram-positive (*Staphylococcus aureus* ATCC 25923, *Staphylococcus aureus* ATCC 6538) bacteria and *Candida albicans* ATCC 10231. The tested PMMA + TOCs foils (20 x 20 mm) prior to antimicrobial study were sterilized using UVC for 15 minutes both sides and treated with visible indoor light, placed in the 12-well plates with 1 mL of microbial inoculum (1.0-4.7 x 10^6 c.f.u. mL^{-1}) in sterile deionized water and incubated for 24h at 37°C in a humid atmosphere and gently shaken (80 r.p.m.) conditions.

Microbial inoculum with a density of 0.5 McFarland (approximately 1.5 x 10^8 c.f.u. mL^{-1}) were prepared in sterile distilled water from cultures of bacterial strains and *C. albicans* grown in tryptic soy broth (TSB, Becton Dickinson) and Sabouraud dextrose broth (SDB, Becton Dickinson), respectively, for 24 hours at 37°C under shaking conditions (120 rpm). Each of microbial inoculum were 100 times diluted prior to use.

Control was the suspension of test microorganisms in the well without test sample. After incubation inoculum was collected from wells, ten-fold diluted and spread (100 μL) on appropriate

 doi:10.20944/preprints202403.1145.v1

medium in Petri dishes. Plates were incubated for 24h at 37°C and colony forming units (c.f.u) were counted on the inoculated plates. Concentration of microorganisms were calculated per one mL

The antimicrobial activity of samples of (**1**) were determined by suspending them in microbial inoculum in sterile deionized water to obtain suspensions with concentrations of 2, 5, 10, and 20% (w/v) and gently mixing (20 r.p.m) using the rotary shaker (Biosan, Latvia) for 24h at 37°C.

Microbial inoculum after treatment with (**1**) samples was ten-fold diluted in sterile deionized water, and each dilution (1000 µL) aseptically mixed with 20 mL of appropriate medium in Petri plates, and incubacted at 37°C for 24h. Colony forming units (c.f.u) were counted and final concentration of microorganisms calculated per one mL.

The antimicrobial activity of powder and composites was determined based on reduction (R) index calculated according to formula: R = Ut – At, where Ut is the common logarithm of the number of microorganisms in the inoculum and At is the common logarithm of the number of microorganisms in the treated inoculum. R ≥ 2 and R ≥ 4 determine biocidal activity of (**1**) in the studied form of composite (antimicrobial activity of the surface) and suspension samples, respectively.

4.4.2. Assessment of Material Cytotoxicity

L929 murine fibroblast cell line (NCTC clone 929) was purchased from American Type Culture Collection (Manassas, VA, USA). The cells were cultured in Dulbecco's Modified Eagle's Medium (DMEM) supplemented with 10% heat-inactivated fetus bovine serum and antibiotics (100 µg/mL of streptomycin and 100 IU/mL of penicillin) at 37°C in an atmosphere of 5% CO_2. All reagents used for cell culture were purchased from VWR International (Radnor, PA, USA).

The specimens were cut into squares measuring 6 mm × 6 mm and were sterilized using UV irradiation for 30 min for each side of the samples before testing.

For evaluation of potential cytotoxicity of tested materials, the samples were placed in individual wells of 24-well plates followed by seeding of cell suspension (1×10^4 cells suspended in a 25 µL of culture medium). Then, the cells were incubated for 4 hours at 37°C and 5% CO_2 to allow cells to attach to the surface of materials before flooding with 1 mL of DMEM medium. L929 cells were incubated on the specimens for 24 and 72 hours at 37°C and 5% CO_2.

After incubation, the samples were transferred to new wells of 24-well plates and 500 µL of the MTT (tetrazolium salt 3-[4,5-dimethylthiazol-2-yl]-2,5-diphenyltetrazolium bromide purchased from Merck KGaA (Darmstadt, Germany)) solution prepared in culture medium without phenol red at a final concentration 0.5 mg/mL was added to each well and kept in an incubator for 3 hours. Then, MTT solution was aspirated and 500 µl of dimethyl sulfoxide was added to each well followed by measurement of the absorbance at 570 nm with the subtraction of the 630 nm background, using a Synergy HT microplate reader (BioTek Instruments, Winooski, VT, USA). MTT assays were repeated in four separate experiments. All values are reported as means ± standard error (SEM). Statistical analysis of the data was performed using two-way analysis of variance (ANOVA) and Duncan test to determine differences in cytotoxicity with the level of significance set at $p < 0.05$.

The analysis of cell numbers growing on the sample surfaces as well as cell morphology was conducted using scanning electron microscopy (SEM; Quanta 3D FEG; Carl Zeiss, Göttingen, Germany). After 24 or 72 hours, cells were washed in PBS and fixed in 2.5% *w/v* glutaraldehyde for 4 hours at 4°C. Subsequently, the specimens were dehydrated in ethanol at increasing concentrations (50%, 75%, 90%, and 100%) for 10 min for each concentration at room temperature. Finally, the specimens were dried and stored at room temperature until the SEM analysis was performed.

5. Conclusions

Crystals of an oxo complex with the general formula $[Ti_8O_2(O^iPr)_{20}(man)_4]$ (**1**) were successfully isolated from the reaction mixture of titanium isopropoxide and mandelic acid, mixed in a molar ratio of 4:1 at room temperature using tetrahydrofuran as a solvent. Structural analysis revealed that the $\{Ti_8O_2\}$ core comprises a central $\{Ti_4O_2\}$ unit and two side dimers ($\{Ti_2\}$), stabilized by two μ_3-O bridges, bridge-forming anions, and a five-membered chelate ring.

 doi:10.20944/preprints202403.1145.v1

Spectral tests including XRD, IR, and Raman spectroscopy confirmed the structural stability of compound (**1**) in both aqueous environments and after incorporation into a polymer matrix. EPR spectroscopy facilitated the detection of reactive oxygen species (ROS) on the surface of the grains (**1**) (in O_2^- form) as well as in the PMMA + (**1**) composite film (in O^- and O_2^- forms).

Biocidal assessments of compound (**1**) and the PMMA + n(**1**) composite were conducted against E. coli and S. aureus bacteria strains, as well as Candida albicans fungi. The antibacterial effect was observed for a suspension containing as little as 2% of (**1**). A suspension containing 20% of (**1**) exhibited biocidal activity against both bacteria and fungi. The bactericidal activity of composite PMMA + (**1**) systems was slightly weaker, moreover they did not show a biocidal effect against fungi.

The observed significant antimicrobial activity of oxo complex (**1**) could stem from the synergetic effects associated with ROS generation and the existence of a chelating ring within its structure. Incorporating (**1**) into the polymer matrix restricted direct interaction with microorganisms, consequently diminishing its antimicrobial efficacy. However, in such instances, the mechanisms linked to ROS generation remain operational. All PMMA + n(**1**) materials demonstated non-cytotoxic characteristic towards L929 fibroblasts.

To sum up, the test results from our investigations affirm that compound (1) fulfills its intended objectives, namely, possessing antibacterial properties while being non-cytotoxic. This compound can be utilized as an antibacterial coating in public facilities or hospitals to mitigate the risk of bacterial infections.

Supplementary Materials: The following supporting information can be downloaded at the website of this paper posted on Preprints.org, Figure S1: The topological analysis of the cluster with $\{Ti_4O_2\}$ core (left) [7] (a), and $\{Ti_8O_2\}$ (**1**) (right) performed in TOPOS [79] (b); Figure S2: EPR spectra obtained for the powdered sample of (**1**) (a) and a cut foil of PMMA + (**1**) 20 wt.% (b). The experimental conditions were as follows: room temperature, microwave frequencies of 9.31648 (a) and 9.32357 (b) GHz; modulation amplitude of 1 mT; sweep width of 20 mT; sweep time of 4 minutes; time constant of 0.1 s; receiver gain of 4 x 10^5; Table S1: Selected bond lengths [Å] and bond angles [°] in (**1**); Table S2. Coordination modes in (**1**).

Author Contributions: A short information specifying their individual contributions of authors : "Conceptualization, P.P., and B.K.; methodology, P.P., T.M., S.W, and B.K.; validation, P.P.; formal analysis, P.P., B.K., G.W., T.M., P.G., and T.J. ; investigation, B.K., G.W., T.M., P.G., and T.J.; resources, B.K.; data curation, P.P., and A.R.; writing—original draft preparation, P.P., and B.K.; writing—review and editing, P.P., A.R., and B.K.; supervision, P.P., A.R., and S.W.; project administration, P.P.; funding acquisition, P.P., A.R., and B.K. All authors have read and agreed to the published version of the manuscript."

Funding: This research received no external funding.

Data Availability Statement: Crystallographic data have been deposited at The Cambridge Crystallographic Data Center via ww.ccdc.cam.ac.uk.data_request/cif. Other data are unavailable due to their potential application meaning.

Conflicts of Interest: The authors declare no conflicts of interest.

References

1. Zhuang, G.; Yan, J.; Wen, Y.; Zhuang, Z.; Yu, Y. Two-Dimensional Transition Metal Oxides and Chalcogenides for Advanced Photocatalysis: Progress, Challenges, and Opportunities. *Sol. RRL* **2021**, *5*, 2000403, doi:10.1002/solr.202000403.
2. Wang, C.; Wang, S.-J.; Kong, F.-G. Calixarene-Protected Titanium-Oxo Clusters and Their Photocurrent Responses and Photocatalytic Performances. *Inorg. Chem.* **2021**, *60*, 5034–5041, doi:10.1021/acs.inorgchem.1c00063.
3. Ni, L.; Liang, D.; Cai, Y.; Diao, G.; Zhou, Z. A Novel Hexanuclear Titanium(IV)-Oxo-Iminodiacetate Cluster with a **Ti** $_6$ **O** $_9$ Core: Single-Crystal Structure and Photocatalytic Activities. *Dalton Trans.* **2016**, *45*, 7581–7588, doi:10.1039/C6DT00031B.
4. Lin, Y.; Zhu, Y.-F.; Chen, Z.-H.; Liu, F.-H.; Zhao, L.; Su, Z.-M. Synthesis, Structure, and Photocatalytic Hydrogen of Three Environmentally Friendly Titanium Oxo-Clusters. *Inorganic Chemistry Communications* **2014**, *40*, 22–25, doi:10.1016/j.inoche.2013.11.023.
5. Kubiak, B.; Piszczek, P.; Radtke, A.; Muzioł, T.; Wrzeszcz, G.; Golińska, P. Photocatalytic and Antimicrobial Activity of Titanium(IV)-Oxo Clusters of Different Core Structure. *Crystals* **2023**, *13*, 998, doi:10.3390/cryst13070998.

6. Janek, M.; Muzioł, T.M.; Piszczek, P. Trinuclear Oxo-Titanium Clusters: Synthesis, Structure, and Photocatalytic Activity. *Materials* **2019**, *12*, 3195, doi:10.3390/ma12193195.
7. Janek, M.; Radtke, A.; Muzioł, T.; Jerzykiewicz, M.; Piszczek, P. Tetranuclear Oxo-Titanium Clusters with Different Carboxylate Aromatic Ligands: Optical Properties, DFT Calculations, and Photoactivity. *Materials* **2018**, *11*, 1661, doi:10.3390/ma11091661.
8. Fenton, J.L.; Laaroussi, A.; Mobian, P.; Chaumont, C.; Khalil, G.; Huguenard, C.; Henry, M. Structural Investigation of Pyridinecarboxylato Titanium(IV) Complexes: An Uncommon Monomeric Octacoordinated Complex vs. a Hexaprismatic Architecture. *Eur J Inorg Chem* **2014**, *2014*, 357–363, doi:10.1002/ejic.201301275.
9. Seisenbaeva, G.A.; Ilina, E.; Håkansson, S.; Kessler, V.G. A New Concept for Titanium Oxo-Alkoxo-Carboxylates' Encapsulated Biocompatible Time Temperature Food Indicators Based on Arising, Not Fading Color. *J Sol-Gel Sci Technol* **2010**, *55*, 1–8, doi:10.1007/s10971-010-2195-8.
10. Benedict, J.B.; Freindorf, R.; Trzop, E.; Cogswell, J.; Coppens, P. Large Polyoxotitanate Clusters: Well-Defined Models for Pure-Phase TiO_2 Structures and Surfaces. *J. Am. Chem. Soc.* **2010**, *132*, 13669–13671, doi:10.1021/ja106436y.
11. Sokolow, J.D.; Trzop, E.; Chen, Y.; Tang, J.; Allen, L.J.; Crabtree, R.H.; Benedict, J.B.; Coppens, P. Binding Modes of Carboxylate- and Acetylacetonate-Linked Chromophores to Homodisperse Polyoxotitanate Nanoclusters. *J. Am. Chem. Soc.* **2012**, *134*, 11695–11700, doi:10.1021/ja303692r.
12. Zhang, L.; Fan, X.; Yi, X.; Lin, X.; Zhang, J. Coordination-Delayed-Hydrolysis Method for the Synthesis and Structural Modulation of Titanium-Oxo Clusters. *Acc. Chem. Res.* **2022**, *55*, 3150–3161, doi:10.1021/acs.accounts.2c00421.
13. Svensson, F.G.; Seisenbaeva, G.A.; Kessler, V.G. Mixed-Ligand Titanium "Oxo Clusters": Structural Insights into the Formation and Binding of Organic Molecules and Transformation into Oxide Nanostructures on Hydrolysis and Thermolysis. *Eur. J. Inorg. Chem.* **2017**, *2017*, 4117–4122, doi:10.1002/ejic.201700775.
14. Wu, R.-H.; Guo, M.; Yu, M.-X.; Zhu, L.-G. Two Titanium(IV)-Oxo-Clusters: Synthesis, Structures, Characterization and Recycling Catalytic Activity in the Oxygenation of Sulfides. *Dalton Trans.* **2017**, *46*, 14348–14355, doi:10.1039/C7DT02516E.
15. Czakler, M.; Artner, C.; Schubert, U. Two New Hexanuclear Titanium Oxo Cluster Types and Their Structural Connection to Known Clusters. *New J. Chem.* **2018**, *42*, 12098–12103, doi:10.1039/C8NJ01077C.
16. Yu, Y.-Z.; Zhang, Y.-R.; Geng, C.-H.; Sun, L.; Guo, Y.; Feng, Y.-R.; Wang, Y.-X.; Zhang, X.-M. Precise and Wide-Ranged Band-Gap Tuning of Ti_6-Core-Based Titanium Oxo Clusters by the Type and Number of Chromophore Ligands. *Inorg. Chem.* **2019**, *58*, 16785–16791, doi:10.1021/acs.inorgchem.9b02951.
17. Guo, Y.-H.; Yu, Y.-Z.; Shen, Y.-H.; Yang, L.-G.; Liu, N.-N.; Zhou, Z.-Y.; Niu, Y.-S. "Three-in-One" Structural-Building-Mode-Based Ti_{16}-Type Titanium Oxo Cluster Entirely Protected by the Ligands Benzoate and Salicylhydroxamate. *Inorg. Chem.* **2022**, *61*, 8685–8693, doi:10.1021/acs.inorgchem.2c00327.
18. Schubert, U. Titanium-Oxo Clusters with Bi- and Tridentate Organic Ligands: Gradual Evolution of the Structures from Small to Big. *Chem. Eur. J.* **2021**, *27*, 11239–11256, doi:10.1002/chem.202101287.
19. Radtke, A.; Piszczek, P.; Muzioł, T.; Wojtczak, A. The Structural Conversion of Multinuclear Titanium(IV) μ-Oxo-Complexes. *Inorg. Chem.* **2014**, *53*, 10803–10810, doi:10.1021/ic5002545.
20. Zheng, Y.-Z.; Zheng, Z.; Chen, X.-M. A Symbol Approach for Classification of Molecule-Based Magnetic Materials Exemplified by Coordination Polymers of Metal Carboxylates. *Coordination Chemistry Reviews* **2014**, *258–259*, 1–15, doi:10.1016/j.ccr.2013.08.031.
21. Rozes, L.; Sanchez, C. Titanium Oxo-Clusters: Precursors for a Lego-like Construction of Nanostructured Hybrid Materials. *Chem. Soc. Rev.* **2011**, *40*, 1006, doi:10.1039/c0cs00137f.
22. Schubert, U. Chemical Modification of Titanium Alkoxides for Sol–Gel Processing. *J. Mater. Chem.* **2005**, *15*, 3701, doi:10.1039/b504269k.
23. Wang, J.-F.; Fang, W.-H.; Li, D.-S.; Zhang, L.; Zhang, J. Cocrystal of $\{Ti_4\}$ and $\{Ti_6\}$ Clusters with Enhanced Photochemical Properties. *Inorg. Chem.* **2017**, *56*, 2367–2370, doi:10.1021/acs.inorgchem.6b02913.
24. Piszczek, P.; Kubiak, B.; Golińska, P.; Radtke, A. Oxo-Titanium(IV) Complex/Polymer Composites—Synthesis, Spectroscopic Characterization and Antimicrobial Activity Test. *IJMS* **2020**, *21*, 9663, doi:10.3390/ijms21249663.
25. Kubiak, B.; Radtke, A.; Topolski, A.; Wrzeszcz, G.; Golińska, P.; Kaszkowiak, E.; Sobota, M.; Włodarczyk, J.; Stojko, M.; Piszczek, P. The Composites of PCL and Tetranuclear Titanium(IV)-Oxo Complexes as Materials Exhibiting the Photocatalytic and the Antimicrobial Activity. *IJMS* **2021**, *22*, 7021, doi:10.3390/ijms22137021.
26. Cui, Y.; Zou, G.-D.; Li, H.-M.; Huang, Y.; Fan, Y. 4-Chlorosalicylate-Stabilized Titanium-Oxo Clusters with Structures Mediated by Tetrazole and Their Photophysical Properties. *Polyhedron* **2019**, *157*, 177–182, doi:10.1016/j.poly.2018.10.011.

27. Luo, W.; Shu, X.-P.; Liu, P.-Y.; Yu, S.-K.; Zhu, Q.-Y.; Dai, J. Lanthanide-Titanium Oxo-Clusters, New Precursors of Multifunctional Colloids for Effective Imaging and Photodynamic Therapy. *Journal of Molecular Liquids* **2020**, *317*, 113946, doi:10.1016/j.molliq.2020.113946.
28. Li, N.; Pranantyo, D.; Kang, E.-T.; Wright, D.S.; Luo, H.-K. A Simple Drop-and-Dry Approach to Grass-Like Multifunctional Nanocoating on Flexible Cotton Fabrics Using In Situ-Generated Coating Solution Comprising Titanium-Oxo Clusters and Silver Nanoparticles. *ACS Appl. Mater. Interfaces* **2020**, *12*, 12093–12100, doi:10.1021/acsami.9b22768.
29. Chen, S.; Fang, W.; Zhang, L.; Zhang, J. Atomically Precise Multimetallic Semiconductive Nanoclusters with Optical Limiting Effects. *Angew Chem Int Ed* **2018**, *57*, 11252–11256, doi:10.1002/anie.201804569.
30. Luo, W.; Hu, B.; Zhang, H.-L.; Li, C.; Shi, Y.; Li, X.; Jin, L. Antibacterial, Photothermal and Stable Ag-Titanium-Oxo-Clusters Hydrogel Designed for Wound Healing. *Materials & Design* **2023**, *226*, 111674, doi:10.1016/j.matdes.2023.111674.
31. De Pasquale, I.; Lo Porto, C.; Dell'Edera, M.; Petronella, F.; Agostiano, A.; Curri, M.L.; Comparelli, R. Photocatalytic TiO2-Based Nanostructured Materials for Microbial Inactivation. *Catalysts* **2020**, *10*, 1382, doi:10.3390/catal10121382.
32. Parcheta, M.; Świsłocka, R.; Świderski, G.; Matejczyk, M.; Lewandowski, W. Spectroscopic Characterization and Antioxidant Properties of Mandelic Acid and Its Derivatives in a Theoretical and Experimental Approach. *Materials* **2022**, *15*, 5413, doi:10.3390/ma15155413.
33. Egner, P.; Pavlačková, J.; Sedlaříková, J.; Pleva, P.; Mokrejš, P.; Janalíková, M. Non-Alcohol Hand Sanitiser Gels with Mandelic Acid and Essential Oils. *IJMS* **2023**, *24*, 3855, doi:10.3390/ijms24043855.
34. Tang, S.-C.; Yang, J.-H. Dual Effects of Alpha-Hydroxy Acids on the Skin. *Molecules* **2018**, *23*, 863, doi:10.3390/molecules23040863.
35. Hou, J.-L.; Luo, W.; Wu, Y.-Y.; Su, H.-C.; Zhang, G.-L.; Zhu, Q.-Y.; Dai, J. Two Ti $_{13}$ -Oxo-Clusters Showing Non-Compact Structures, Film Electrode Preparation and Photocurrent Properties. *Dalton Trans.* **2015**, *44*, 19829–19835, doi:10.1039/C5DT03153B.
36. Ding, Q.-R.; Liu, J.-X.; Narayanam, N.; Zhang, L.; Zhang, J. Construction of Molecular Rectangles with Titanium–Oxo Clusters and Rigid Aromatic Carboxylate Ligands. *Dalton Trans.* **2017**, *46*, 16000–16003, doi:10.1039/C7DT03470A.
37. Huang, Y.; Zou, G.-D.; Li, H.-M.; Cui, Y.; Fan, Y. A Photoactive {Ti $_{16}$ } Metal–Organic Capsule: Structural, Photoelectrochemical and Photocatalytic Properties. *New J. Chem.* **2018**, *42*, 14079–14082, doi:10.1039/C8NJ02992J.
38. Kemmitt, T.; Al-Salim, N.I.; Gainsford, G.J.; Bubendorfer, A.; Waterland, M. Unprecedented Oxo-Titanium Citrate Complex Precipitated from Aqueous Citrate Solutions, Exhibiting a Novel Bilayered Ti $_{8}$ O $_{10}$ Structural Core. *Inorg. Chem.* **2004**, *43*, 6300–6306, doi:10.1021/ic049760r.
39. Salam, A.; Dadzie, O.E.; Galadari, H. Chemical Peeling in Ethnic Skin: An Update. *Br J Dermatol* **2013**, *169 Suppl 3*, 82–90, doi:10.1111/bjd.12535.
40. Gentili, G.; Perugini, P.; Bugliaro, S.; D'Antonio, C. Efficacy and Safety of a New Peeling Formulated with a Pool of PHAs for the Treatment of All Skin Types, Even Sensitive. *J Cosmet Dermatol* **2023**, *22*, 517–528, doi:10.1111/jocd.15215.
41. Dębowska, R.M.; Kaszuba, A.; Michalak, I.; Dzwigałowska, A.; Cieścińska, C.; Jakimiuk, E.; Zielińska, J.; Kaszuba, A. Evaluation of the Efficacy and Tolerability of Mandelic Acid-Containing Cosmetic Formulations for Acne Skin Care. *pd* **2015**, *4*, 316–321, doi:10.5114/dr.2015.53419.
42. Greive, K.; Tran, D.; Townley, J.; Barnes, T. An Antiaging Skin Care System Containing Alpha Hydroxy Acids and Vitamins Improves the Biomechanical Parameters of Facial Skin. *CCID* **2014**, 9, doi:10.2147/CCID.S75439.
43. Świsłocka, R.; Świderski, G.; Nasiłowska, J.; Sokołowska, B.; Wojtczak, A.; Lewandowski, W. Research on the Electron Structure and Antimicrobial Properties of Mandelic Acid and Its Alkali Metal Salts. *IJMS* **2023**, *24*, 3078, doi:10.3390/ijms24043078.
44. Mamdouh S Masoud; Alaa E Ali; Almaza A Shokry; Sherif A. Kolkaila Chelation and Molecular Structure of Mandelic Acid Complexes. *Journal of Chemical Research Advances* **2021**, *02*, 1–9.
45. Youzhu, Y.; Hui, W.; Leilei, L.; Yuhua, G.; Jing, F.; Yichao, L. Crystal Structure of Bis(μ $_{2}$ -2-Oxido-2-Phenylacetato-κ ^{3} *O*,*O*′:*O*′)-Bis(*N* -Oxido-Benzamide-κ ^{2} *O*,*O*′)-Bis(Propan-2-Olato-κ ^{1} *O*)Dititanium(IV), C $_{36}$ H $_{38}$ N $_{2}$ O $_{12}$ Ti $_{2}$. *Zeitschrift für Kristallographie - New Crystal Structures* **2022**, *237*, 957–959, doi:10.1515/ncrs-2022-0326.
46. Youzhu, Y.; Yuhua, G.; Yongsheng, N.; Nana, L.; Hongfei, Z. Crystal Structure of Bis(μ $_{2}$ -2-Oxido-2-Phenylacetate-κ ^{3} *O* : *O* , *O* ′)-Bis(1-Isopropoxy-2-Oxo-2-Phenylethan-1-Olato-κ ^{2} O,O′)-Bis(Propan-2-Olato-κ ^{1} O)Dititanium(IV), C $_{44}$ H $_{52}$ O $_{14}$ Ti $_{2}$. *Zeitschrift für Kristallographie - New Crystal Structures* **2021**, *236*, 467–469, doi:10.1515/ncrs-2020-0590.
47. Schetter, B.; Stosiek, C.; Ziemer, B.; Mahrwald, R. Multinuclear Enantiopure Titanium Self-Assembly Complexes—Synthesis, Characterization and Application to Organic Synthesis. *Appl. Organometal. Chem.* **2007**, *21*, 139–145, doi:10.1002/aoc.1183.

48. Addison, A.W.; Rao, T.N.; Reedijk, J.; Van Rijn, J.; Verschoor, G.C. Synthesis, Structure, and Spectroscopic Properties of Copper(II) Compounds Containing Nitrogen–Sulphur Donor Ligands; the Crystal and Molecular Structure of Aqua [1,7-Bis(N-Methylbenzimidazol-2′-Yl)-2,6-Dithiaheptane]Copper(II) Perchlorate. *J. Chem. Soc., Dalton Trans.* **1984**, 1349–1356, doi:10.1039/DT9840001349.
49. Macrae, C.F.; Sovago, I.; Cottrell, S.J.; Galek, P.T.A.; McCabe, P.; Pidcock, E.; Platings, M.; Shields, G.P.; Stevens, J.S.; Towler, M.; et al. *Mercury 4.0* : From Visualization to Analysis, Design and Prediction. *J Appl Crystallogr* **2020**, *53*, 226–235, doi:10.1107/S1600576719014092.
50. Cicco, S.; Vona, D.; Gristina, R.; Sardella, E.; Ragni, R.; Lo Presti, M.; Farinola, G. Biosilica from Living Diatoms: Investigations on Biocompatibility of Bare and Chemically Modified Thalassiosira Weissflogii Silica Shells. *Bioengineering* **2016**, *3*, 35, doi:10.3390/bioengineering3040035.
51. Xue, F.; Janzen, D.M.; Knecht, D.A. Contribution of Filopodia to Cell Migration: A Mechanical Link between Protrusion and Contraction. *International Journal of Cell Biology* **2010**, *2010*, 1–13, doi:10.1155/2010/507821.
52. Piszczek, P.; Richert, M.; Grodzicki, A.; Głowiak, T.; Wojtczak, A. Synthesis, Crystal Structures and Spectroscopic Characterization of [Ti8O8(OOCR)16] (Where R=But, CH2But, C(CH3)2Et). *Polyhedron* **2005**, *24*, 663–670, doi:10.1016/j.poly.2005.01.014.
53. Frot, T.; Cochet, S.; Laurent, G.; Sassoye, C.; Popall, M.; Sanchez, C.; Rozes, L. Ti $_{8}$ O $_{8}$ (OOCR) $_{16}$, a New Family of Titanium–Oxo Clusters: Potential NBUs for Reticular Chemistry. *Eur. J. Inorg. Chem.* **2010**, *2010*, 5650–5659, doi:10.1002/ejic.201000807.
54. Fan, X.; Yuan, F.; Li, D.; Chen, S.; Cheng, Z.; Zhang, Z.; Xiang, S.; Zang, S.; Zhang, J.; Zhang, L. Threefold Collaborative Stabilization of Ag $_{14}$ -Nanorods by Hydrophobic Ti $_{16}$ -Oxo Clusters and Alkynes: Designable Assembly and Solid-State Optical-Limiting Application. *Angew. Chem. Int. Ed.* **2021**, *60*, 12949–12954, doi:10.1002/anie.202101664.
55. Wang, S.; Reinsch, H.; Heymans, N.; Wahiduzzaman, M.; Martineau-Corcos, C.; De Weireld, G.; Maurin, G.; Serre, C. Toward a Rational Design of Titanium Metal-Organic Frameworks. *Matter* **2020**, *2*, 440–450, doi:10.1016/j.matt.2019.11.002.
56. Kim, B.; Keum, Y.; Chen, Y.-P.; Oh, H.S.; Lee, J.Y.; Park, J. Stimuli-Responsive Ti-Organic Gels and Aerogels Derived from Ti-Oxo Clusters: Hierarchical Porosity and Photocatalytic Activity. *Inorg. Chem.* **2019**, *58*, 15936–15941, doi:10.1021/acs.inorgchem.9b02444.
57. Czakler, M.; Artner, C.; Schubert, U. Influence of the Phosphonate Ligand on the Structure of Phosphonate-Substituted Titanium Oxo Clusters. *Eur. J. Inorg. Chem.* **2013**, *2013*, 5790–5796, doi:10.1002/ejic.201300859.
58. Fan, X.; Fu, H.; Gao, M.-Y.; Zhang, L.; Zhang, J. One-Pot and Postsynthetic Phenol-Thermal Synthesis toward Highly Stable Titanium-Oxo Clusters. *Inorg. Chem.* **2019**, *58*, 13353–13359, doi:10.1021/acs.inorgchem.9b02238.
59. Liu, J.-X.; Gao, M.-Y.; Fang, W.-H.; Zhang, L.; Zhang, J. Bandgap Engineering of Titanium-Oxo Clusters: Labile Surface Sites Used for Ligand Substitution and Metal Incorporation. *Angew. Chem. Int. Ed.* **2016**, *55*, 5160–5165, doi:10.1002/anie.201510455.
60. Wu, Y.-Y.; Luo, W.; Wang, Y.-H.; Pu, Y.-Y.; Zhang, X.; You, L.-S.; Zhu, Q.-Y.; Dai, J. Titanium–Oxo–Clusters with Dicarboxylates: Single-Crystal Structure and Photochromic Effect. *Inorg. Chem.* **2012**, *51*, 8982–8988, doi:10.1021/ic301092b.
61. He, W.; Liu, Y.; Wamer, W.G.; Yin, J.-J. Electron Spin Resonance Spectroscopy for the Study of Nanomaterial-Mediated Generation of Reactive Oxygen Species. *Journal of Food and Drug Analysis* **2014**, *22*, 49–63, doi:10.1016/j.jfda.2014.01.004.
62. Xiong, L.-B.; Li, J.-L.; Yang, B.; Yu, Y. Ti 3 + in the Surface of Titanium Dioxide: Generation, Properties and Photocatalytic Application. *Journal of Nanomaterials* **2012**, *2012*, 1–13, doi:10.1155/2012/831524.
63. Suriye, K.; Lobo-Lapidus, R.J.; Yeagle, G.J.; Praserthdam, P.; Britt, R.D.; Gates, B.C. Probing Defect Sites on TiO2 with [Re3(CO)12H3]: Spectroscopic Characterization of the Surface Species. *Chem. Eur. J.* **2008**, *14*, 1402–1414, doi:10.1002/chem.200701514.
64. Dan-Hardi, M.; Serre, C.; Frot, T.; Rozes, L.; Maurin, G.; Sanchez, C.; Férey, G. A New Photoactive Crystalline Highly Porous Titanium(IV) Dicarboxylate. *J. Am. Chem. Soc.* **2009**, *131*, 10857–10859, doi:10.1021/ja903726m.
65. Richards, E.; Murphy, D.M.; Che, M. An EPR Characterisation of Stable and Transient Reactive Oxygen Species Formed under Radiative and Non-Radiative Conditions. *Res Chem Intermed* **2019**, *45*, 5763–5779, doi:10.1007/s11164-019-04001-0.
66. Śmigiel, J.; Piszczek, P.; Wrzeszcz, G.; Jędrzejewski, T.; Golińska, P.; Radtke, A. The Composites of PCL and Tetranuclear Titanium(IV)–Oxo Complex with Acetylsalicylate Ligands—Assessment of Their Biocompatibility and Antimicrobial Activity with the Correlation to EPR Spectroscopy. *Materials* **2022**, *16*, 297, doi:10.3390/ma16010297.
67. Vaishampayan, A.; Grohmann, E. Antimicrobials Functioning through ROS-Mediated Mechanisms: Current Insights. *Microorganisms* **2021**, *10*, 61, doi:10.3390/microorganisms10010061.

68. Mazur, P.; Skiba-Kurek, I.; Mrowiec, P.; Karczewska, E.; Drożdż, R. Synergistic ROS-Associated Antimicrobial Activity of Silver Nanoparticles and Gentamicin Against Staphylococcus Epidermidis. *IJN* **2020**, *Volume 15*, 3551–3562, doi:10.2147/IJN.S246484.
69. Lam, P.-L.; Wong, R.S.-M.; Lam, K.-H.; Hung, L.-K.; Wong, M.-M.; Yung, L.-H.; Ho, Y.-W.; Wong, W.-Y.; Hau, D.K.-P.; Gambari, R.; et al. The Role of Reactive Oxygen Species in the Biological Activity of Antimicrobial Agents: An Updated Mini Review. *Chemico-Biological Interactions* **2020**, *320*, 109023, doi:10.1016/j.cbi.2020.109023.
70. Joe, A.; Park, S.-H.; Kim, D.-J.; Lee, Y.-J.; Jhee, K.-H.; Sohn, Y.; Jang, E.-S. Antimicrobial Activity of ZnO Nanoplates and Its Ag Nanocomposites: Insight into an ROS-Mediated Antibacterial Mechanism under UV Light. *Journal of Solid State Chemistry* **2018**, *267*, 124–133, doi:10.1016/j.jssc.2018.08.003.
71. Beyene, B.B.; Mihirteu, A.M.; Ayana, M.T.; Yibeltal, A.W. Synthesis, Characterization and Antibacterial Activity of Metalloporphyrins: Role of Central Metal Ion. *Results in Chemistry* **2020**, *2*, 100073, doi:10.1016/j.rechem.2020.100073.
72. Chen, S.; Wu, G.; Zeng, H. Preparation of High Antimicrobial Activity Thiourea Chitosan–Ag+ Complex. *Carbohydrate Polymers* **2005**, *60*, 33–38, doi:10.1016/j.carbpol.2004.11.020.
73. Burns, J.; McCoy, C.P.; Irwin, N.J. Synergistic Activity of Weak Organic Acids against Uropathogens. *Journal of Hospital Infection* **2021**, *111*, 78–88, doi:10.1016/j.jhin.2021.01.024.
74. Tshuva, E.Y.; Peri, D. Modern Cytotoxic Titanium(IV) Complexes; Insights on the Enigmatic Involvement of Hydrolysis. *Coordination Chemistry Reviews* **2009**, *253*, 2098–2115, doi:10.1016/j.ccr.2008.11.015.
75. Immel, T.A.; Grützke, M.; Batroff, E.; Groth, U.; Huhn, T. Cytotoxic Dinuclear Titanium-Salan Complexes: Structural and Biological Characterization. *Journal of Inorganic Biochemistry* **2012**, *106*, 68–75, doi:10.1016/j.jinorgbio.2011.08.029.
76. E. CrysAlis Red and CrysAlis CCD. Oxford Diffraction Ltd. Abingdon, Oxfordshire, 2000.
77. Sheldrick, G.M. Crystal Structure Refinement with *SHELXL*. *Acta Crystallogr C Struct Chem* **2015**, *71*, 3–8, doi:10.1107/S2053229614024218.
78. Brandenburg, K. Berndt, M. Diamond, Release 2.1e, Crystal Impact GbR, Bonn, Germany, 2001.
79. Blatov, V.A.; Shevchenko, A.P.; Proserpio, D.M. Applied Topological Analysis of Crystal Structures with the Program Package ToposPro. *Crystal Growth & Design* **2014**, *14*, 3576–3586, doi:10.1021/cg500498k.